Drying of Complex Suspensions

Lei Xu (徐磊),[1,2] Alexis Bergès,[3] Peter J. Lu (陸述義),[2] André R. Studart,[4] Andrew B. Schofield,[5] Hidekazu Oki (沖秀一),[6] Simon Davies,[7] and David A. Weitz[2]

[1]*Department of Physics, The Chinese University of Hong Kong, Shatin, Hong Kong*
[2]*Department of Physics and SEAS, Harvard University, Cambridge, Massachusetts 02138, USA*
[3]*Département de physique, École Normale Supérieure, 75005 Paris, France*
[4]*Complex Materials, Department of Materials, ETH Zurich, 8093 Zurich, Switzerland*
[5]*The School of Physics, University of Edinburgh, Edinburgh EH9 3JZ, United Kingdom*
[6]*Shinagawa-ku, 141-0032 Tokyo, Japan*
[7]*AkzoNobel Corporate, R320 Wilton Centre, Redcar TS104RF, United Kingdom*

(Received 29 July 2009; published 24 March 2010)

We investigate the 3D structure and drying dynamics of complex mixtures of emulsion droplets and colloidal particles, using confocal microscopy. Air invades and rapidly collapses large emulsion droplets, forcing their contents into the surrounding porous particle pack at a rate proportional to the square of the droplet radius. By contrast, small droplets do not collapse, but remain intact and are merely deformed. A simple model coupling the Laplace pressure to Darcy's law correctly estimates both the threshold radius separating these two behaviors, and the rate of large-droplet evacuation. Finally, we use these systems to make novel hierarchical structures.

DOI: 10.1103/PhysRevLett.104.128303 PACS numbers: 47.57.−s, 47.55.N−, 47.56.+r

The drying of suspensions of colloidal particles gives rise to a plethora of fascinating phenomena, from the ''coffee-ring'' effect [1] to episodic crack propogation [2] and the fractal patterns arising from invasion percolation [3]. Drying of colloidal suspensions is also important technologically: paints and other coatings depend on colloidal particles for many of their key properties, many ceramics go through a stage of particle drying, and cosmetics often exploit the unique properties of colloidal-scale particles, particularly for such beneficial properties as screening the harmful effects of the sun. However, for many of these technological applications, the colloidal particles are but one of many different components, and drying of the colloids is accompanied by many other phase changes. While these mixtures can become highly complex, a simpler, yet still rich system that embodies many of the complex phenomena of these technological suspensions is a mixture of immiscible fluids with a colloidal suspension; a simple example is a mixture of an emulsion and colloidal particles. The behavior of the emulsion embodies many of the archetypal phenomena of such systems, while still remaining sufficiently tractable to enable it to be fully understood. However, emulsions themselves typically scatter light significantly, and when mixed with a colloidal suspension, this scattering is only enhanced. As a result, it is very difficult to image this mixture, precluding optical studies of its behavior, and knowledge of the actual behavior is woefully missing.

In this Letter, we explore the drying of mixtures of aqueous emulsion droplets and spherical colloidal particles with confocal microscopy, which allows us to resolve the full 3D structure of these mixtures and their temporal dynamics. We find that the particles first jam into a solidified pack, throughout which emulsion drops are dispersed; a front of air then passes through the entire system. When this drying front reaches large emulsion droplets, the droplets unexpectedly collapse and their internal contents are forced into the pore space between the surrounding colloids, driven by an imbalance of pressures at the droplets' interfaces with air and with the solvent. By contrast, small droplets are deformed by the drying front, yet remain intact without bursting. By coupling the Laplace pressure with Darcy's law for flow through a porous medium, we predict the duration of large-droplet invasion, and show that the threshold size between bursting and deformation is comparable to the size of the colloidal particles. We use this technique to create novel hierarchical materials.

We suspend sterically stabilized colloidal spheres of polymethylmethacrylate (PMMA) with radius $r_p = 1\ \mu$m in decahydronaphthalene (DHN). Separately, we create an emulsion of an aqueous phase, comprising equal volumes of water and glycerol, and PGPR-90 surfactant, required for droplet stability, in the nonpolar DHN; our homogenizer creates polydisperse droplets ranging from microns to tens of microns. We combine particle suspension and emulsion to create our particle-droplet mixtures. These particular components ensure that the refractive indices of the particles, droplets and background solvent are all sufficiently matched that we can image the entire bulk of the 3D structure with confocal fluorescence microscopy, with single-particle resolution [4]. To distinguish particles from droplets, we use different dyes: particles are dyed with nitrobenzoxadiazole (NBD) and appear green; droplets are dyed with rhodamine-B and appear red. We deposit the particle-droplet mixture on a clean glass coverslip, and image with an inverted confocal microscope

(Leica SP5). The droplets are coated immediately by colloids, reminiscent of a pickering emulsion [5]. As in the case of particle-only systems, evaporation proceeds in two stages [3]. First, particles and droplets are driven toward the edge of the drying sample, where they jam, analogous to the coffee-ring effect in particle-only systems [1]. Then, a drying air front invades the jammed system and displaces the DHN, which ultimately evaporates completely; we do not observe cracks during drying, as expected for particles of this size [3]. We use confocal microscopy to observe the particle-droplet mixture after jamming, as the drying front passes through, which allows us to determine the exact size and position of each emulsion droplet and colloidal particle [4]. A 3D reconstruction of a typical jammed mixture before drying is shown in Fig. 1(a), with droplets and particles shown in red and green, respectively. Collecting this full 3D data takes several seconds, far too slow to observe the rapid dynamics that occur during air invasion; instead, to capture these dynamics, we fix the focal plane in the bulk of the sample and collect high-speed 2D images every 70 ms. By imaging the same regions in 3D first, then rapidly in 2D as the air invades, we can observe the drying process with good spatial and temporal resolution.

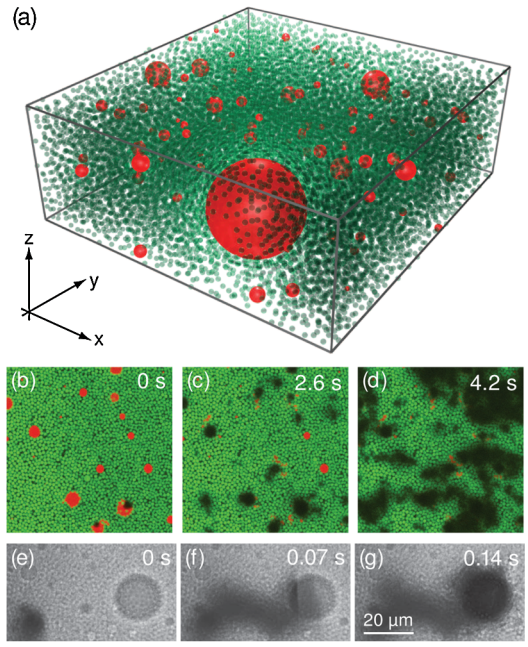

FIG. 1 (color online). Structure and drying of droplet-particle mixtures. (a) Reconstruction of a typical sample from confocal microscope images, with dimensions $91 \times 91 \times 30\ \mu\text{m}^3$. Polydisperse red spheres are emulsion droplets; monodisperse green spheres are PMMA particles, shown at half size for clarity. (b)–(d) Two-dimensional confocal microscope images in x-y plane, within the bulk of the sample, showing the invasion of the drying front. (b) Onset of air invasion. (c) As the drying front moves through, emulsion droplets turn black first, followed by (d) air invading the particle regions. (e)–(g) Bright-field images showing droplet invasion, where air appears black and the solvent is transparent. Air (e) approaches, (f) contacts, and (g) rapidly evacuates the droplet.

In the jammed configurations before air invasion, the emulsion droplets are distributed throughout the colloidal particles, as shown in Fig. 1(a). As the sample dries, more and more particle regions turn black; the invading air displaces the solvent around the particles, destroying the refractive index match, as illustrated in Figs. 1(b)–1(d). The droplets also turn black as drying proceeds, but whether they are replaced by air or solvent cannot be resolved with fluorescence, where both appear black. We therefore observe droplet invasion with bright-field transmission microscopy, where the solvent remains transparent but air appears black. We observe that droplets are replaced by material that appears black in bright field, which therefore must be air, as shown in Figs. 1(e)–1(g). For a more detailed understanding of droplet behavior, we observe large isolated emulsion droplets, with radii R_d greater than a few microns, during drying. Because it is energetically unfavorable to displace the preexisting organic solvent, which wets the PMMA particles, with the aqueous droplet fluid that does not, we expect that the aqueous fluid remains in the droplet and slowly evaporates upon contact with air, with very little fluid motion. Contrary to this expectation, however, we instead observe significant fluid motion: air rapidly forces the contents of the droplet into the pore space between the surrounding particles, leaving an empty, spherical void, as shown in Figs. 2(a)–2(c). This flow cannot occur spontaneously; instead, a strong driving force must exist.

To understand this driving force, we analyze the distribution of pressures inside and around an isolated droplet. The total pressure near an interface is determined by a combination of the external pressure and the interface's Laplace pressure. The magnitude of the Laplace pressure is usually estimated as the ratio of the interfacial tension to interface's curvature radius; its sign is positive for convex interfaces, negative for concave. Before air invasion, the droplet is surrounded by particles and solvent, as shown in Fig. 2(d). The air protrudes into the solvent, making a concave profile with a negative Laplace pressure, as shown in Fig. 2(e) [2]. We estimate P_{solv}, the pressure of the solvent, as the difference between atmospheric pressure P_{atm}, and the Laplace pressure of the air-solvent interface, as shown in Fig. 2(e): $P_{\text{solv}} \cong P_{\text{atm}} - \sigma_{\text{air|solv}}/a$, where $\sigma_{\text{air|solv}}$ is the interfacial tension of the air-solvent interface, and a is the typical size of the pores between colloidal particles. The tiny pore size produces large negative Laplace pressures, and hence a low P_{solv}. As a result, the droplet is surrounded by a low-pressure environment.

At the interface between droplet and solvent, the aqueous droplet protrudes into the nonpolar solvent around the colloids, as shown in Fig. 2(f); the Laplace pressure here is therefore positive. We estimate the pressure inside the droplet as $P_1 \cong P_{\text{solv}} + \sigma_{\text{drop|solv}}/a$, where $\sigma_{\text{drop|solv}}$ is the interfacial tension of the droplet-solvent interface.

As soon as air touches the droplet, however, the pressure distribution changes dramatically. In particular, part of the

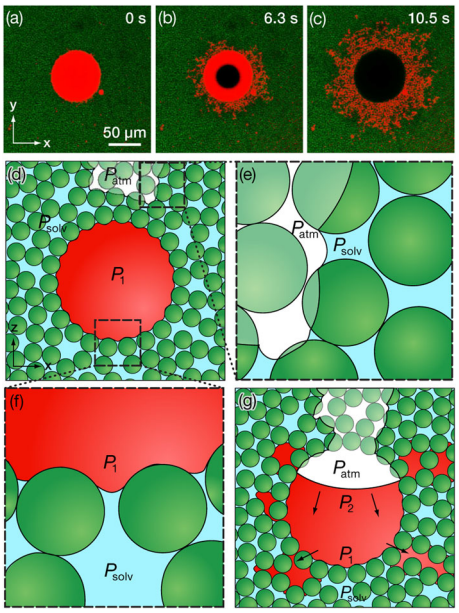

FIG. 2 (color online). (a)–(c) Confocal microscope images of the air invasion of a large-droplet viewed at a fixed x-y plane, where air forces the contents of the droplet into the surrounding colloids. Before air invasion, tiny projections of the droplet extend into the surrounding pores, visible in (a). (d) Schematic in the x-z plane showing the pressure distribution before air (white) touches the droplet. Enlargement of the (e) air-solvent and (f) droplet-solvent interfaces. (g) Schematic of the pressure distribution during evacuation. Inside the droplet, the region next to air-droplet interface has a high pressure P_2; the region next to solvent-droplet interface has a low pressure P_1. The difference between these pressures drives the flow of droplet contents into the surrounding particles.

droplet is now in contact with the much-higher atmospheric air pressure, as illustrated in Fig. 2(g). Near the air-droplet interface, the pressure inside the drop is estimated to be $P_2 \cong P_{\text{atm}} - \sigma_{\text{air|drop}}/R_d$, where we have approximated the radius of air-droplet interface by the droplet size R_d. The pressure near the droplet-solvent interface remains P_1, as illustrated in Fig. 2(g). If $P_2 > P_1$, then the pressure difference ΔP will force droplet fluid into the surrounding pore space between colloidal particles:

$$\Delta P = P_2 - P_1 \cong \frac{\sigma_{\text{air|solv}}}{a} - \frac{\sigma_{\text{air|drop}}}{R_d} - \frac{\sigma_{\text{drop|solv}}}{a}, \quad (1)$$

where any change in solvent pressure across the droplet is negligible. Interestingly, ΔP depends not on atmospheric pressure, but rather on the competition between the Laplace pressures at the various interfaces. We measure the corresponding surface tensions with the pendant drop method: $\sigma_{\text{air|solv}} = 26 \pm 2$ mN/m, $\sigma_{\text{air|drop}} = 51 \pm 3$ mN/m, and $\sigma_{\text{drop|solv}} = 3.8 \pm 0.3$ mN/m. Because of the presence of surfactant at the interface, the droplet-solvent surface tension $\sigma_{\text{drop|solv}}$ is so much lower than the other two that its contribution to the overall pressure difference is negligible. The radii that we measure for the large droplets, $R_d \cong 10$–50 μm, are orders of magnitude larger than the size of the interparticle pore space, $a \cong 0.36 r_p = 0.36$ μm for random close-packed particles [6]. Consequently, the contribution from a pressure drop across the air-droplet interface is also small; the flow is driven by the low pressure in the solvent evacuating the large drops, as shown in Figs. 2(a)–2(c). Since the solvent strongly wets the particles, the menisci of the air evaporating the solvent from the pores creates a low pressure in the solvent. Reflected in the first term in Eq. (1), this establishes the large pressure difference that drives the flow. We estimate $\Delta P \cong 0.6$ atm for these large drops.

The high time resolution afforded by the rapid collection of 2D image sequences in the confocal microscope allows us to measure t_{ev}, the evacuation time for air to invade the large droplets and force their contents into the surrounding particles; t_{ev} varies for droplets of different sizes. We measure the size of each droplet from the initial 3D confocal data, then quantify t_{ev} using fast 2D images of droplet evacuation. Collected deep in the bulk of the sample, our images are large enough to contain a number of droplets to obtain good statistics, yet are small enough relative to the sample size to achieve a uniform sampling environment. We find that the variation of t_{ev} with R_d is consistent with a power law, albeit over less than a decade. The exponent is approximately 2, as shown by the comparison of the line with the points on the log-log plot in Fig. 3(a).

We estimate this relationship theoretically with a simple model based on Darcy's Law for fluid flow in a porous medium [7] to determine a characteristic evacuation velocity, $v_{\text{ev}} = \kappa \nabla P/\mu$, where κ is the permeability of the porous medium, and μ is the dynamic viscosity of the fluid. We estimate ∇P, the pressure gradient that drives the aqueous fluid into the porous medium, as the characteristic pressure difference divided by the droplet diameter, $\nabla P = \Delta P/2R_d$. We then estimate $t_{\text{ev}} \cong 2R_d/v_{\text{ev}}$, yielding $t_{\text{ev}} = \frac{4\mu}{\kappa \Delta P} R_d^2$.

The model predicts that t_{ev} data follow an R_d^2 dependence; indeed, the experimental data closely conform to this particular power-law scaling, as shown on the log-log plot in Fig. 3(a). Moreover, we can further test the model by estimating the prefactor $4\mu/(\kappa \Delta P)$. We estimate κ using the Kozeny-Carman equation for flow through a porous medium [8], $\kappa \cong r_p^2(1-\phi)^3/(45\phi^2)$, where the pore size is determined by the particle volume fraction ϕ. From the 3D particle positions in the bulk, we measure $\phi = 0.63 \pm 0.03$, consistent with random close packing; however, around the large droplets, the particles are hexagonally close packed, and the next layer tightly packs the interstices, as illustrated in Figs. 3(b)–3(d). We think these well-ordered particles predominantly determine the pore size through which the droplets evacuate, and therefore estimate the permeability using the higher $\phi = 0.74$. We measure $\mu = 8.9 \pm 0.1$ mPa-s for the H_2O/glycerol mixture, yielding our rough estimate of $4\mu/(\kappa \Delta P) \approx 0.8 \times 10^9$ s/m^2; this value is of the same order as the value

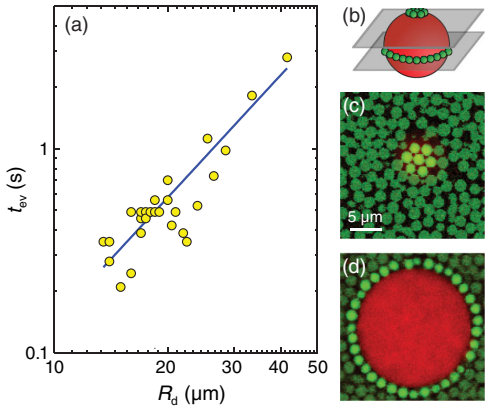

FIG. 3 (color online). (a) Measurement of droplet evacuation duration time, t_{ev}, as a function of droplet radius, R_d, for a typical drying experiment. For the measured half decade, the data are consistent with a power-law of slope 2. (b) Schematic of 2D images representing slices through a droplet at different heights. (c) Confocal microscope image at the top of the droplet, showing the hexagonal crystalline ordering of the particles that suggests $\phi \approx 0.74$. (d) Confocal microscope image through the droplet center, showing the dense packing around the droplet, consistent with high ϕ. In these images, the brightness of the particles in contact with the droplet has been enhanced for clarity.

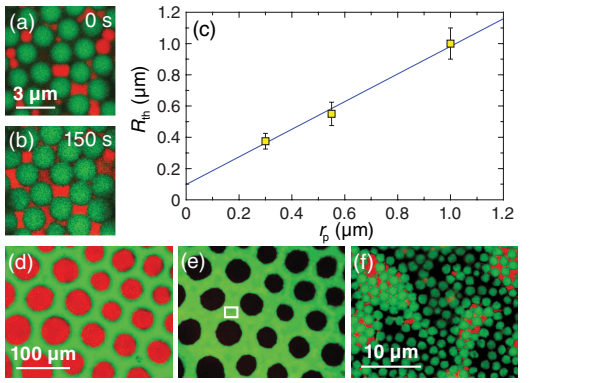

FIG. 4 (color online). (a)–(c) Behavior of small droplets during drying. Small droplets are (a) deformed but not invaded, and eventually (b) coalesce to form a continuous phase. (c) The threshold droplet radius, R_{th}, vs the particle radius, r_p. A linear fit through the data points, $R_{th} = (0.88 \pm 0.16)r_p + (0.1 \pm 0.1)$, consistent with our prediction $R_{th} = 0.83r_p$. (d)–(f) Hierarchical porous material created from drying. Structure made from $R_d \cong 20$ μm droplets and $r_p = 1$ μm particles (d) before air invasion, and (e) after invasion. (f) Enlargement of the compact region marked by the box in (e). The particles appear nonspherical because of the difference in their refractive index relative to air. The system contains pores of two characteristic sizes: voids from droplets (20 μm) and interparticle pores (0.5 μm).

of $t_{ev}/R_d^2 = 1.2 \times 10^9$ s/m^2 from the fit to the experimental data in Fig. 3(a), and provides support that our model captures the correct physics.

Our model explains the air invasion of large droplets, whose contents are forced into the surrounding pore space. It also implies a completely different behavior for sufficiently small droplets: as R_d decreases, ΔP must also decrease, as can be seen from Eq. (1). Eventually, for sufficiently small drop size, ΔP will become zero and will no longer drive any flow; the high Laplace pressure of these small droplets makes them so stiff that they cannot be invaded by air. Indeed, when we observe small droplets prepared by ultrasonic homogenization, we find that the small droplets are not invaded by air but instead are simply deformed and pushed into pore space between the surrounding particles, as shown in Figs. 4(a) and 4(b).

We estimate the threshold radius R_{th}, beneath which droplets will not be invaded by air by using the previous values for the parameters in Eq. (1) and solving for $\Delta P = 0$; our model predicts that $R_{th} = 2.30a = 0.83r_p$. To test this prediction, we measure R_{th} for droplets mixed with particles of several different radii, varying r_p by more than half an order of magnitude. We find the dependence $R_{th} = (0.88 \pm 0.16)r_p + (0.1 \pm 0.1)$, in excellent agreement with the prediction of our model, as shown in Fig. 4(c).

We observe two qualitatively different behaviors: droplets that evacuate and collapse, creating large voids; and droplets that remain intact during drying, yielding void-free particle packs. We use this dichotomy to produce hierarchical materials with several different controllable length scales, by varying droplet and particle sizes. One such structure, using droplets with $R_d \cong 20$ μm and particles with $r_p = 1$ μm, is shown in Figs. 4(d)–4(f). The resulting hierarchical porous material has voids of two length scales: 20 μm, from droplets, and 0.5 μm, from the pore space between particles. Hierarchical materials may be useful in making low-density porous materials or to mimic hierarchical natural structures; our evacuation results demonstrate drying as a general low-energy method to drive desired materials into a porous medium.

We gratefully acknowledge support from the NSF (DMR-0602684), Harvard MRSEC (DMR-0213805), RGC Research Grant Direct Allocation (Project Code: 2060395), NASA (NNX08AE09G), Pixar and ICI.

[1] R. D. Deegan *et al.*, Nature (London) **389**, 827 (1997).
[2] E. R. Dufresne *et al.*, Phys. Rev. Lett. **91**, 224501 (2003).
[3] L. Xu *et al.*, Phys. Rev. Lett. **101**, 094502 (2008).
[4] P. J. Lu *et al.*, Nature (London) **453**, 499 (2008).
[5] O. D. Velev *et al.*, Langmuir **12**, 2374 (1996).
[6] H. J. Frost, Office of Naval Research, Contract N00014-77-C-0002 NR-039-136, Tech. Report 6 (1978).
[7] G. K. Batchelor, *Introduction to Fluid Dynamics* (Cambridge University Press, Cambridge, England, 2000), p. 234.
[8] P. C. Carman, *Flow of Gases through Porous Media* (Butterworth, London, 1956).